A cross-method comparison of sub-10 nm nanoparticle size distribution

Ye Yang,[†] Suiyang Liao,[‡] Zhi Luo,[‡] Runzhang Qi,[†] Niamh Mac Fhionnlaoich,[†]
Francesco Stellacci,[‡,¶] and Stefan Guldin[*,†]

[†]*Department of Chemical Engineering, University College London, Torrington Place, London WC1E 7JE, U.K.*

[‡]*Institute of Materials, École Polytechnique Fédérale de Lausanne, 1015 Lausanne, Switzerland*

[¶]*Interfaculty Bioengineering Institute, École Polytechnique Fédérale de Lausanne, 1015 Lausanne, Switzerland*

E-mail: s.guldin@ucl.ac.uk

Abstract

Accurate nanoparticle (NP) size determination is essential across research domains, with many functions in nanoscience and biomedical research being size-dependent. Although transmission electron microscopy (TEM) is capable of resolving a single NP down to the sub-nm scale, the reliable representation of entire populations is plagued by challenges in providing statistical significance, predominantly due to limited sample counts, suboptimal preparation procedures and operator bias during image acquisition and analysis. Meanwhile alternative techniques exist, but reliable implementation requires a detailed understanding of appendant limitations. Herein, conventional TEM is compared to the size determination of sub-10 nm gold NPs in solution by small-angle X-ray scattering and analytical ultracentrifugation. Form-free Monte Carlo fitting of scattering profiles offers access to a direct representation of the core size distribution while ultracentrifugation sedimentation velocity analysis provides information of the hydrodynamic size distribution. We report a comparison of these three methods in determining the size of quasi-monodisperse, polydisperse and bimodal gold nanoparticles of 2 – 7 nm and discuss advantages and limitations of each technique.

Keywords

nanoparticle, SAXS, TEM, AUC, Monte Carlo

Introduction

The preparation and accurate characterization of sub-10 nm nanoparticles (NPs) plays a pivotal role in a multitude of chemical and biomedical applications, where size-dependent efficacy is often observed.[1–3] Notably, the cutoff for efficient renal clearance is below 10 nm, and NPs with broad size distributions may impair biocompatibility.[4] For gold nanoparticles (AuNPs), in particular, various important physicochemical properties are closely dependent on size. AuNP populations with mean diameters ranging from 2 – 10 nm manifest drastic differences not only concerning *in vitro* colloidal stability but also their intracellular and antimicrobial properties.[5–8] Consequently, the quantitative assessment of the AuNP size distribution in a sample of interest is an indispensable routine that needs particular attention.

The most commonly implemented technique is transmission electron microscopy (TEM) imaging, combined with a plethora of software-based image analysis methods.[9,10] As a direct imaging technique, TEM is a convenient tool to study both size and shape in ultra-high resolution. However, obtaining an accurate and representative size distribution of the AuNPs by TEM is challenged by limited sample counts, preparation procedures and operator bias in image acquisition and analysis.[11–13] Considering the rather limited sample size, it is laborious to obtain results of statistical significance, especially for non-uniform or multimodal samples. Moreover, the drop casting for TEM sample preparation often results in drying artifacts, which vastly complicates image analysis.[14,15] Even though fitting procedures with minimal human intervention meanwhile exist,[10] image analysis in practice still commonly involves manual operations prone to user bias. While cryo-TEM and liquid-phase TEM offer mitigation and present exciting pathways for NP research, accessibility is limited. With the current experimental workflows, their implementation in routine use for size characterization remains unfeasible.[13,16]

To address these issues, a number of bulk-scale quantification techniques for NPs have been developed as alternatives to TEM imaging. For instance, dynamic light scattering (DLS) is widely used for its ease of access and simple protocol. Whilst DLS is able to probe the hydrodynamic size information of colloidal systems at both microscopic and nanoscopic scales, non-monodisperse samples are typically not accurately described due to the size-dependent scattering cross-section. Thus, smaller NPs are usually overshadowed by larger NPs or aggregates.[11,17] In addition, the interference of multiple scattering events may also impair the accuracy of DLS results. For AuNPs below 20 nm, it is therefore extremely challenging to obtain reliable results with DLS.[18] X-ray diffraction (XRD) analysis enables to obtain the mean size of crystalline domains, either via the Scherrer formula or the more recent Fourier inversion method.[19,20] However, this approach is unable to represent particle size distributions and is challenged by issues such as the overweighting of larger crystallites as well as contributions from amorphous layers and lattice defects.[14,21] Nanoparticle tracking analysis (NTA) allows to size each NP in an ensemble through the mapping of individual Brownian trajectories.[22] Per contra, it is challenging to resolve sub-10 nm NPs and to obtain large enough datasets for an accurate representation of NP populations.[18]

Analytical ultracentrifugation (AUC) offers an alternative route to size and shape characterization of NPs in solution through an accurate determination of the velocity during sedimentation. Unlike the sedimentation equilibrium (SE) mode in which a moderate centrifugal force is applied to achieve an equilibrium between sedimentation and back diffusion, the sedimentation velocity (SV) mode relies on high centrifugal fields that result in steep concentration gradients.[23] While in principle being a simple and versatile technique, the utilization of AUC is still highly underrepresented in NP research. One of the main reasons is attributed to the difficulty in determining the effective NP density for core-shell hybrid colloids, since a solvation layer in addition to the ligand shell can pose significant influence. This challenge was addressed with a 2D evaluation of sedimentation and diffusion coefficients, which permitted the direct estimation of the size, density and molecular weight distributions of AuNPs stabilized by a thiol ligand shell.[24] Further developments shared a focus on modern algorithms for the analysis of core-shell properties as well as polydisperse systems.[25,26] However, the AUC representation of non-uniform or multimodal NPs remains largely unexplored.

Another emerging technique to characterize the size distribution of colloidal ensembles is small-angle X-ray scattering (SAXS). With a momentum transfer q of $0.06 - 6.3\,\mathrm{nm}^{-1}$, SAXS measurements are able to cover the NP size distribution ranging from $1 - 100\,\mathrm{nm}$ in diameter. Moreover, gold has a pronounced scattering length density (SLD) of $125 \times 10^{-6}\,\text{Å}^{-2}$ for Cu-source X-ray while the SLDs for H_2O and alkanethiols are below $10 \times 10^{-6}\,\text{Å}^{-2}$. This distinct feature of gold gives rise to significant contrast and excellent signal-to-noise ratio for resulting AuNP SAXS profiles. Contrary to TEM analysis, SAXS is an indirect method and requires data correction and fitting for reconstructing the size distribution from measured data.[27] In principle, the size distribution of a NP sample can be directly calculated with an assumed functional form, i.e. lognormal, Gaussian, Boltzmann or Schultz-Zimm distribution.[12] For the accurate representation of any kind of size distribution, a form-free regularization approach based on indirect Fourier transform has been widely adopted to probe colloidal systems in solution, involving form factor pattern matching and optimization with least-squares methods.[28–30] In a recent comparative study for sub-5 nm hybrid NPs, SAXS demonstrated compelling advantages to DLS and fluorescence correlation spectroscopy by resolving not only the size distribution of the silica core but also the molecular mass dispersity of the polymer shell via quantitative modeling with a core-shell sphere form factor.[31] Nonetheless, the parametric regularization methods are sensitive to prior information such as the maximum diameter, which may occur artificial oscillations.[32] To this end, a Monte Carlo (MC) method, based on model-free trial-and-error sampling, was proposed for unbiased NP size distribution analysis.[33,34] Although this iterative process requires substantial computing power, MC fitting exhibits a rather simple theoretical structure since it assumes the scattered intensity is approximated by the sum of elementary components, i.e. for SAXS the Rayleigh scattering functions of homogeneous spheres.[35] This approach was pioneered by Martelli and Di Nunzio, who demonstrated comparable sizing capabilities to the established indirect Fourier transform, structure interference and maximum entropy methods.[33] However, this pathway was limited to spherical systems, which severely restricted its further application. A refined algorithm was developed by Pauw et al. by compensating the effect of size and shape on the scaling of the form factors, which extended the use in polydisperse ensembles with unknown shapes.[34,36] Importantly, the recent development of the user-friendly software McSAS has further broadened the scope of this approach.[37,38] In a cross-lab collaboration of unimodal 5 nm AgNP, the parametric fitting and the MC method led to consistent and similar results, highlighting the validity and reliability of employing the MC approach.[39] The consistency between the presupposed model fitting and the MC method was further confirmed in a study of unimodal PbS nanocrystals in the range of $3-10$ nm.[40] Despite these encouraging results, there remains a lack of comprehensive investigations utilizing the MC-SAXS method, especially for characterizing non-uniform NPs below 10 nm as well as in direct comparison with other characterization techniques.

To this end, we present a cross-method comparative study of quasi-monodisperse, polydisperse and bimodal thiol-capped AuNPs of $2-7$ nm between conventional TEM and solution-based SAXS and AUC. The three techniques are based on fundamentally different working principles, i.e. direct imaging, scattering and sedimentation. We present feasible routes to obtain experimental data from all three techniques and provide a side-by-side comparison of the size distribution obtained from data analysis for a variety of samples. By doing so, we aim to shed light on the general applicability of MC-SAXS and AUC-SV methods for accurate NP size determination alongside a critical identification of their limitations.

Materials and methods

Preparation of gold nanoparticles. The 11-mercapto-1-undecanesulfonate (MUS) ligand[41] and MUS-AuNP synthesis via oleylamine (OAm) ligand exchange[42] were carried out following previously published procedures. Four batches of MUS-AuNPs were synthesized with varying reaction temperatures at 40, 25, 15, 10 °C and labeled as MUS-NP1 − NP4, respectively. We refer to the Supporting Information for experimental details.

Transmission electron microscopy characterization. The TEM samples were prepared by dipping a sample grid (Holey Carbon Film on Copper 400 mesh, EM Resolutions) into AuNPs solutions in dichloromethane (DCM). TEM images were acquired with a high-resolution JEM-2100 TEM system (200 keV, JEOL). The size distribution was determined by automated image analysis of the respective AuNP populations (count rates >2000) using the software ImageJ. The size and circularity threshold were set as $>2\,\mathrm{nm}^2$ and >0.6, respectively. To assess the reproducibility of TEM analysis, three individual sample grids were prepared from each of MUS-NP1 and MUS-NP4 sample solutions. Subsequent TEM imaging was performed in three separate experimental sessions.

Small-angle X-ray scattering measurements and Monte Carlo fitting. Samples for solution-based SAXS were prepared in 10 mM NaCl aqueous solution at a concentration of 5 mg/ml for MUS-NP1–4 and $10\,\mathrm{mg\,ml^{-1}}$ for MUS-B1–B2. The SAXS measurements were carried out using a Ganesha 300XL (SAXSLAB) at 20 °C under vacuum with a high brilliance microfocus Cu-source (wavelength: 1.5418 Å). The SAXS data were recorded on a Pilatus 300K solid-state photon-counting detector with a 2 mm beam stop for 1 h (q-range: 0.015 to $0.65\,\text{Å}^{-1}$). After subtracting the scattering from the 10 mM NaCl buffer solution, the

SAXS data were fed into the software McSAS (version 1.3) for size distribution analysis.[37] In McSAS, the fitting of each SAXS dataset consisted of 10 individual repetitions with strict fitting criteria, namely a convergence criterion of $\chi^2 < 1$ and a minimum uncertainty estimate of 2%. Sphere model was chosen as the fit model and the ΔSLD (= $\mathrm{SLD_{Au}} - \mathrm{SLD_{H_2O}}$) was input as $115.5 \times 10^{-6}\,\text{Å}^{-2}$. Number-weighted histograms were generated in the post-fit analysis. The number of bins was set to be 100 in a size range of 1.8 − 9.0 nm in diameter.

Analytical ultracentrifugation characterization. The AUC-SV measurements were carried out using an Optima XL-A Ultracentrifuge (Beckman Coulter) for diluted SAXS sample solutions (with 10 mM NaCl). Concentrations were adjusted to lie in the range 0.2 − 0.4 mg/ml, which corresponded to 0.5 − 1.0 OD, as confirmed by a pre-scan of UV-Vis absorption at 400 nm for each sample before the SV measurement. The recorded AUC data were processed in the software SEDFIT to derive approximate solutions to the Lamm equation via a numerical finite element method.[43] This fitting process generated a smooth sedimentation coefficient distribution $c(s)$ for each sample. Extended 2D analysis was performed to calculate the weighted average sedimentation s and diffusion coefficients D based on average effective density using a previously published custom made MATLAB code.[24]

Results and discussion

Homo-ligand AuNPs stabilized by MUS were prepared via thiol-for-OAm ligand exchange from four batches of differently-sized AuNPs that were initially protected by OAm.[42] As summarized in Tab S1, the core size of the four batches ranged from 2 − 7 nm and varying degrees of size dispersity. Two binary mixtures were prepared by mixing MUS-NP1 and MUS-NP4 at weight ratios of 1:1 and 1:5, labeled as MUS-B1 and MUS-B2, respectively (Tab S2).

TEM imaging

TEM size histograms of MUS-NP1 and MUS-NP4 from three separate experimental sessions for both sample preparation and imaging are shown in Fig 1 alongside a normalized overlay and representative micrographs. The count rate for each individual analysis was > 2000.

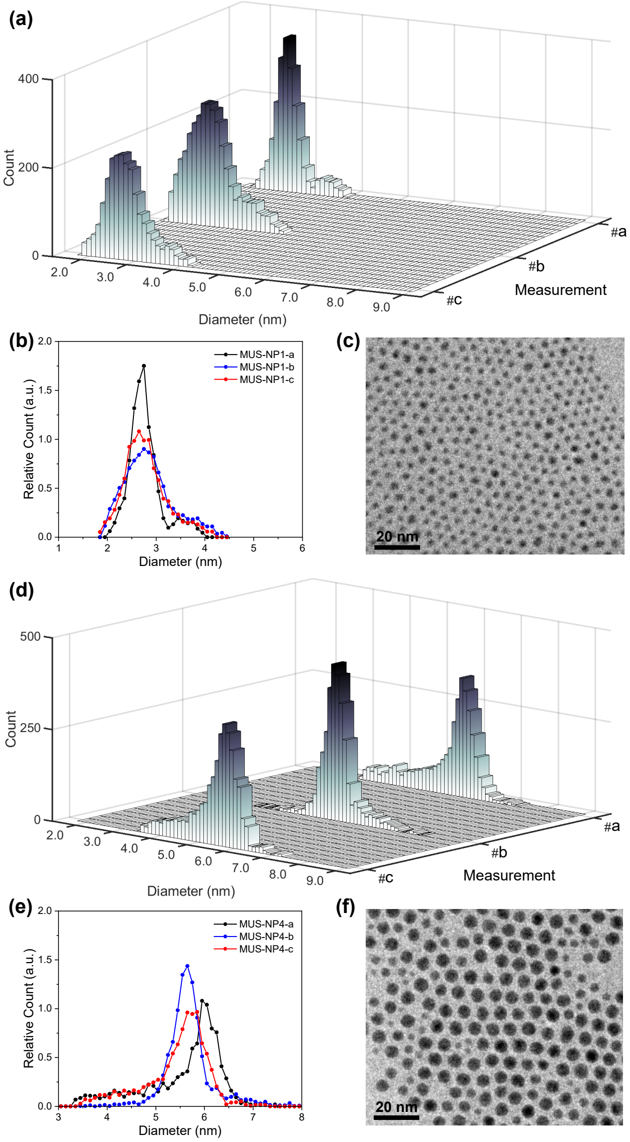

Figure 1: Size distribution histograms, normalized overlays and representative TEM image of MUS-NP1 (a-c) and MUS-NP4 (d-f). Three histograms were obtained per batch of AuNPs in three separate experiments (sample preparation and acquisition) from the identical sample solution.

For MUS-NP1, the obtained histograms are reasonably well represented by a normal distribution (see Supporting Information Fig S1a), yielding mean size and standard deviation of 2.8 ± 0.3, 2.9 ± 0.5 and 2.8 ± 0.4 for the three respective analyses and corresponding dispersity values of 12.4 %, 17.7 % and 15.9 %. These significant differences are also depicted in the normalized overlays of the respective histograms, shown in Fig 1b. Further evidence for the disparity of the three sub-populations is provided by direct statistical comparison, namely the t-test and the Kolmogorov-Smirnov test. The t-test assumes that both sub-populations follow a normal distribution with equal variance and determines whether the two groups have the same mean, i.e. originate from the same parental population. The corresponding p-values of the pairwise comparison are shown in the Supporting Information, with MUS-NP1-a and MUS-NP1-c likely originating from the same parental population, while the null hypothesis was rejected for all other couples, i.e. there were significant differences detected between the respective sub-populations. The more generic two-sample Kolmogorov-Smirnov test was also applied to determine whether the respective pairs of sub-populations follow the same distribution. The obtained p-values were orders of magnitude below the significance level of 5%, suggesting that none of the sub-population would, from a statistical perspective, originate from the same AuNP population. Overall these results indicate that the variation in sample preparation and analysis is statistically significant. See the Supporting Information for details.

A similar comparative analysis of the respective TEM experiments is presented for MUS-NP4 in Fig 1d-f. It is important to note that the above conducted (and widely common) reporting of mean values, standard deviation and dispersity represents a simplification and is not suitable for size populations that deviate from normal distributions.[44] As shown in the Supporting Information (Fig S1b), the MUS-NP4 sub-populations displayed herein cannot be described by a normal distribution. Nevertheless, significant differences are also apparent from qualitative comparison, most notably by the lack of a shoulder towards smaller AuNPs in MUS-NP4-b compared to MUS-NP4-a and MUS-NP4-c. Furthermore, the position of the main peak ranges from 5.6 nm to 6.0 nm between the three runs. Both, t-test and Kolmogorov-Smirnov were also applied to MUS-NP4-a, MUS-NP4-b and MUS-NP4-c, yielding stark evidence that the three respective sub-populations are significantly different from a statistical perspective (see Supporting Information)

These findings are in agreement with earlier studies, emphasizing on the limitations of TEM size analysis when based on the conventional practice of sample preparation and image analysis applied herein.[27,45]

MC-SAXS analysis

The SAXS profiles of both single-type samples and binary mixtures were measured in aqueous solutions. For a better estimation of the form factor of individual AuNPs, 10 mM NaCl was added to increase the ionic strength of the medium and thus screen any medium- and long-range interaction between AuNPs. SAXS curves after background subtraction are presented as log-log plots in Fig 2 for 5 mg/ml single-type solutions and 10 mg/ml binary mixtures, respectively. Qualitatively, both single-type and biomodal measured curves demonstrated pronounced form peaks in the high q region and featureless flat profiles for $q < 1\,\mathrm{nm}^{-1}$.

For single-type samples, the peak position of the form peak in the high q region was at 3.2, 2.8, 2.2 and $1.9\,\mathrm{nm}^{-1}$ for MUS-NP1 – NP4, respectively (Fig 2a-d). This clear shift towards lower angles corresponds to a size increase of the scatterer, which was in line with the TEM results. Meanwhile, the curves of the binary mixtures followed closely the pattern overlapping of individual form peaks observed in single-type samples (Fig 2e,f).

Both, the date fitting of single-type and binary mixtures indicate that effective scattering occurred from individual AuNPs with non-interacting contributions, which we relate to three major factors: 1) the distinct SLD of gold gave rise to pronounced form factors in diluted solutions, 2) the ionic repulsion by MUS maintained excellent colloidal stability and prevented NP clustering or aggregation, 3) the addition of 10 mM NaCl resulted in charge screening, which disrupted medium- and long-range NP-NP ionic interaction. It is important to note

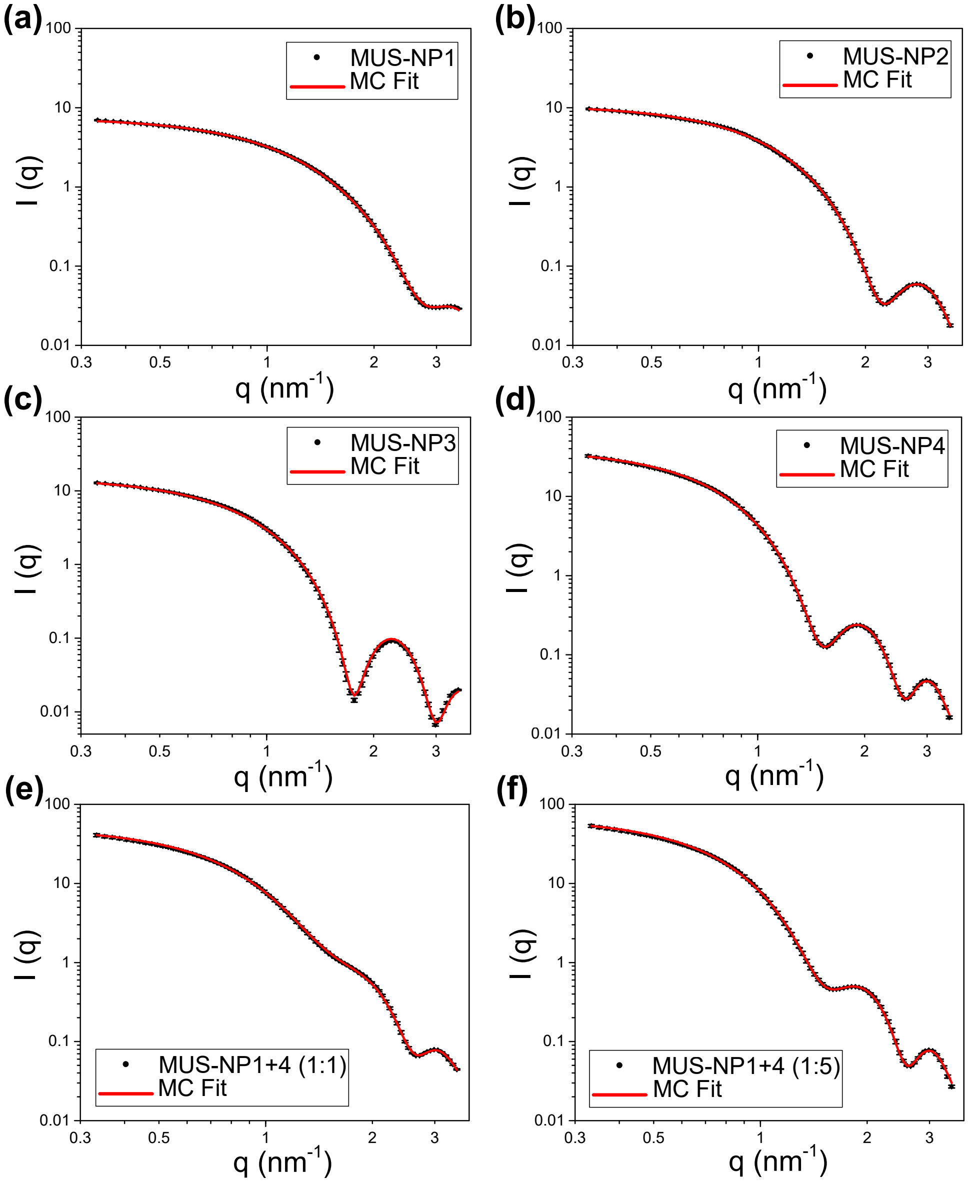

Figure 2: SAXS profiles and MC fitting (log-log plots) of (a) 5 mg/ml MUS-NP1, (b) 5 mg/ml MUS-NP2, (c) 5 mg/ml MUS-NP3, (d) 5 mg/ml MUS-NP4, (e) 10 mg/ml MUS-B1 (1:1_{wt}) and (f) 10 mg/ml MUS-B2 (1:5_{wt}).

that these features were key prerequisites for the implementation of MC fitting analysis. A summary of statistical information obtained from 10 number-weighted output distributions by independent MC fitting repetitions for each sample is shown in the Supporting Information (Tab S3). Note the closely matched fitting curves and the negligible discrepancies between individual runs. These results indicate that the herein presented MC-SAXS method provides robust results for non-monodisperse and bimodal AuNP populations with minimal external information.

AUC-SV analysis

The sedimentation of NPs relates to their size, shape and density. Herein, the procedure of an AUC-SV measurement alongside numerical finite element fitting in SEDFIT allowed to retrieve the 1D sedimentation coefficient distribution $c(s)$ and deconvolute D from the s profile to generate 2D $c(s, D)$ information for a more comprehensive analysis. The representative results are shown in Fig 3 for MUS-B2. Further results for separate samples of MUS-NP1 and MUS-NP4 are provided in the Supporting Information (Fig S2). Characterization of MUS-NP1 gave rise to a primary peak at 48 S (Svedberg unit, equals to 10^{-13} s) and a less pronounced secondary peak at 77 S. Both peaks were also retrieved in the 2D plot with matched peak position and relative intensity. By contrast, although the 1D analysis of MUS-NP4 resolved a dominant peak at 204 S and a much reduced peak at 141 S, the secondary peak was diminished after 2D analysis, which required experimental data of higher signal-to-noise ratio. Two peaks at 58 S and 198 S, respectively, were well resolved in both 1D and 2D plots of the mixed sample MUS-B2.

Importantly, with MUS-B2 being a mixture of MUS-NP1 and MUS-NP4 ($1{:}5_{\mathrm{wt}}$), both peaks can be assigned to the primary peaks in the single-type solutions. Meanwhile, no further distribution feature was extracted from the 2D analysis, suggesting a potential loss of information such as the secondary peaks of the respective native populations MUS-NP1 and MUS-NP4. Our results are in line with a recent study by Walter et al., who related the lack of sensitivity to the regularization process and the simplified treatment of applying a global average density in the 2D sedimentation-diffusion analysis, ignoring the size dependence of ρ_{eff}.[26]

Due to the above observed limitations of the 2D sedimentation-diffusion analysis, the results of the 1D sedimentation served to calculate the size distribution. Please see the Supporting Information for a full overview of the hydrodynamic size analysis. In short, the

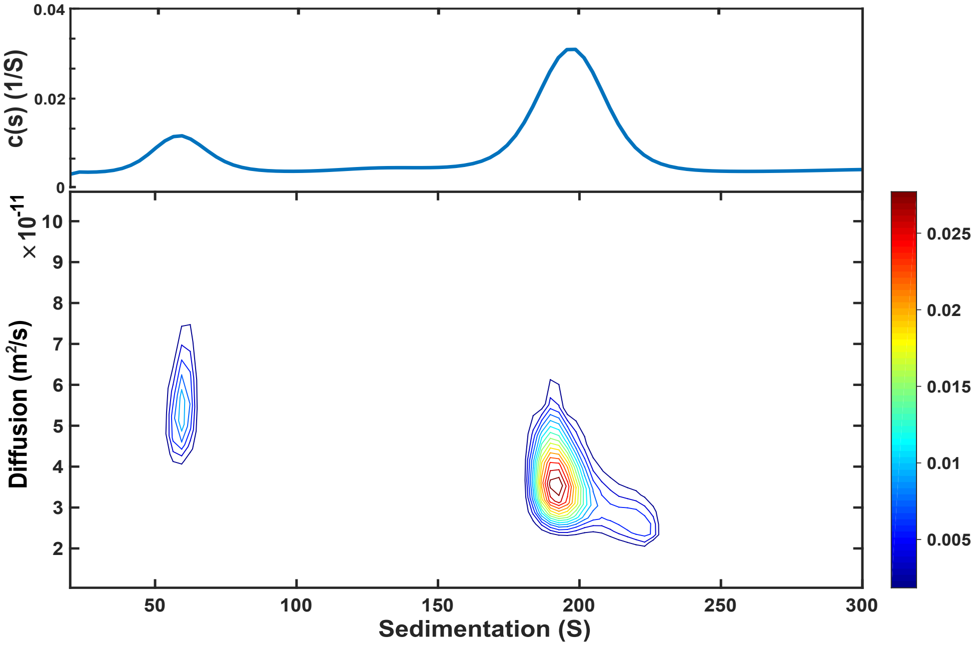

Figure 3: Sedimentation and diffusion analysis of MUS-B2 (1:5$_{\mathrm{wt}}$). Two plots correspond to the integral 1D sedimentation coefficient distribution and the 2D sedimentation-diffusion correlation.

d_{H} obtained from the Stokes-Einstein equation (Eq S1) was related to core-shell model (Fig S3) consisting of a rigid gold core of diameter d and a soft shell of thickness l formed by the MUS ligand capping and a solvation layer. The effective density ρ_{eff} of MUS-AuNPs with hydrodynamic diameter d_{H} was then calculated for each sample. The derived d_{H} vs. $c(s)$ relationships are summarized in Fig S4 and the results are exemplified by the plot for MUS-B2 in Fig 4(a). Since the AUC data was represented by absorbance, the $c(s)$ data was corrected by the extinction coefficient ε to compensate for size-dependent Rayleigh scattering and absorption.[46,47] The size dependence of NP extinction coefficient (black dots, based on[46]) and corrected distribution plots (green) for MUS-B2 are summarized in Fig 4(b), with results for the other samples shown in Fig S4. Note the significant increase in the number fraction of the smaller-sized AuNPs as a consequence of the extinction compensation.

It is important to note that for retrieving the core size distribution of AuNPs with the implemented 1D approach, a fixed value for l was used to account for both the ligand capping layer and the solvation layer, here 1.3 nm according to published results on an identical NP

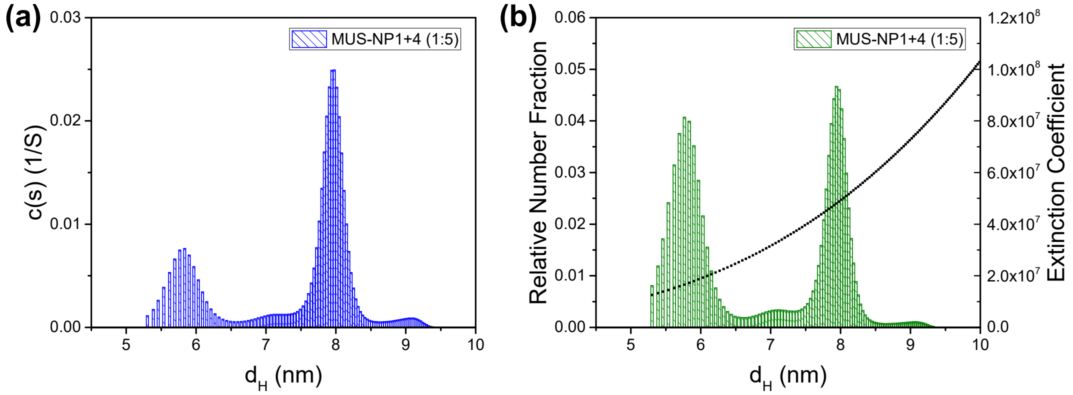

Figure 4: Calculated size distribution before (a) and after (b) extinction correction of MUS-B2 (1:5_{wt}) by AUC-SV. The extinction coefficient of the gold core as a function of size is shown in black scatters.

system.[48] While this is a simplified approximation, the ample contrast between the gold core and the soft shell layer still renders this method transferable to many NP systems which have rigid cores and smooth surface morphologies.

Comparative studies

Fig 5 summarizes the size distribution histograms obtained from TEM imaging, MC-SAXS and AUC-SV for the single-type samples MUS-NP1 − NP4, containing AuNPs ranging from 2 − 7 nm. Some important characteristics emerge from a direct comparison.

As evidenced by the Gaussian fit plotted alongside Figs 5g,h,i, the results obtained for MUS-NP3 by all three techniques follow a normal distribution, thus enabling to reliably compare mean size and standard deviation from statistical analysis. The obtained mean size was remarkably similar, with 5.0 nm, 5.1 nm, and 5.0 nm calculated for TEM imaging, MC-SAXS and AUC-SV, respectively. The spread of counts was broader in TEM analysis with a standard deviation of 0.3 nm in comparison to 0.2 nm obtained for both MC-SAXS and

AUC-SV. The corresponding dispersity was calculated alongside with 6.8 %, 3.9 %, 3.4 %, respectively.

Apart from MUS-NP1 (Fig 5a-c), where the MC-SAXS result was discrepant to TEM and AUC-SV, the position of the main peak was consistent for all AuNP populations across the three techniques. In general for AuNPs below 3 nm, MC-SAXS provided a less defined spread and higher error values. The existence of shoulders or minority populations was found more pronounced in TEM than in MC-SAXS and AUC-SV, but all techniques picked up some degree of dispersity. In particular for MUS-NP1 and MUS-NP4, the main peak obtained by AUC-SV was significantly narrower than for the other techniques.

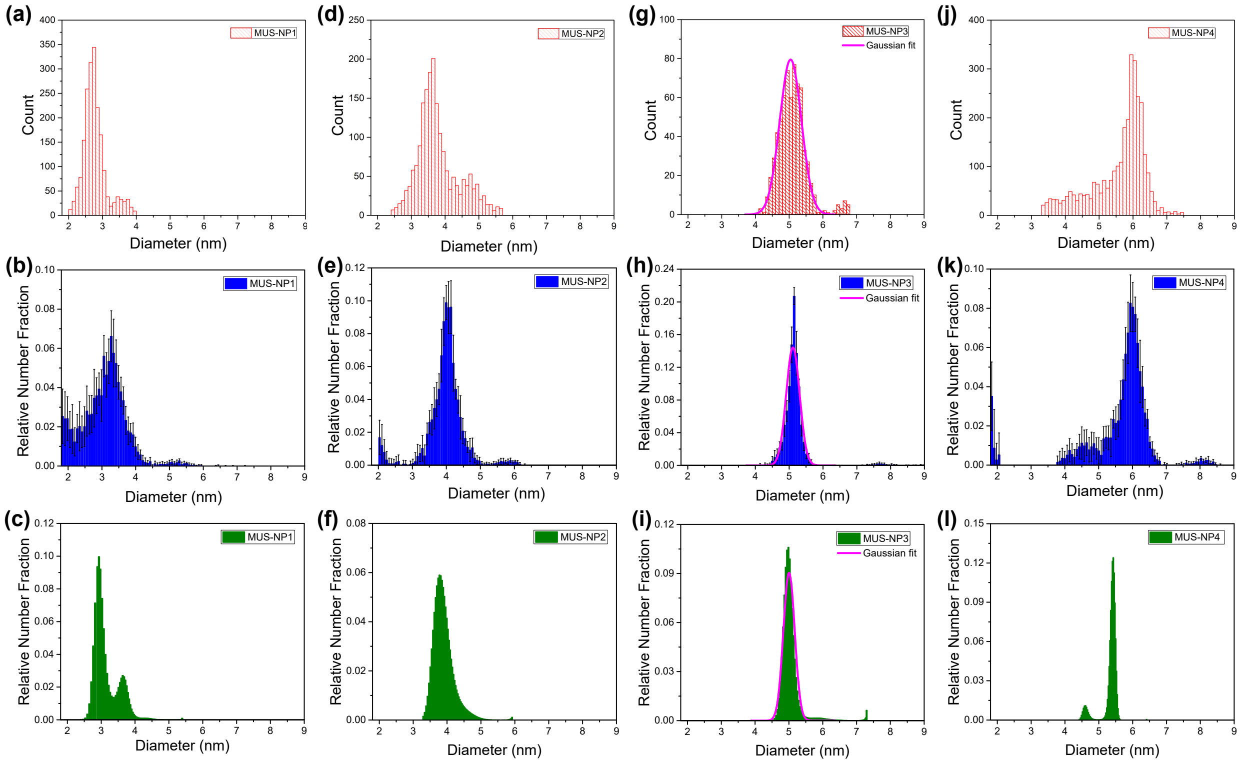

Figure 5: Size distribution analysis of single-type samples by TEM (red), SAXS (blue) and AUC (green): (a)–(c) MUS-NP1, (d)–(f) MUS-NP2, (g)–(i) MUS-NP3, (j)–(l) MUS-NP4. To represent core size distribution, $2\times l$ were subtracted for the AUC results after normalization with corresponding extinction coefficients.

These trends were also observed in the binary mixtures MUS-B1 and MUS-B2, as shown in Fig 6. A comparison of the data to expected simulated histograms via superposition of the single-type results can be found in the Supporting Information (Fig S5). Most notably, the AUC-SV characterization was unable to accurately represent the minority population in MUS-B1, where a equal weight mixture of MUS-NP1 and MUS-NP4 and thus a dominance of MUS-NP1 in numbers effectively led to an overshadowing of the larger, less numerous AuNPs.

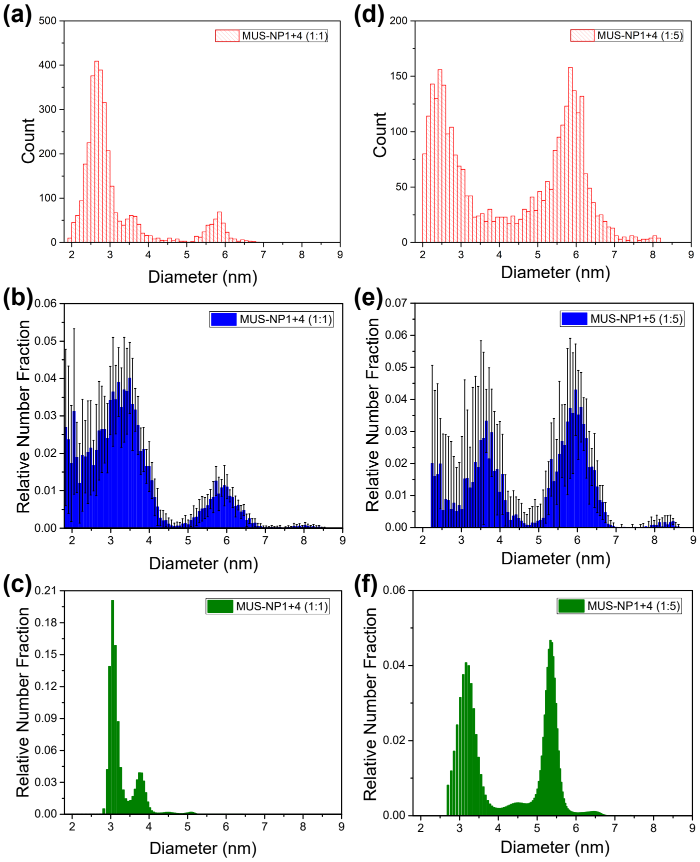

Figure 6: Size distribution analysis of binary mixtures by TEM (red), SAXS (blue) and AUC (green): (a)–(c) MUS-B1 ($1{:}1_{\mathrm{wt}}$), (d)–(f) MUS-B2 ($1{:}5_{\mathrm{wt}}$). To represent core size distribution, $2\times l$ were subtracted for the AUC results after normalization with corresponding extinction coefficients.

The following discussion aims to systematically examine the advantages and limitations of each techniques. In all samples, the variation between individual characterization runs for the identical sample was observed to be significantly higher for TEM compared to SAXS and AUC. This may be related to the fact that 1) TEM is a local imaging technique, which carries limited statistical representation by examining only a small fraction of the whole sample population; 2) The inspection of single particles and the experimenter-guided workflow of sample preparation, imaging and data analysis can entail errors from operator bias.[12,13] Furthermore, it is important to mention that although we have seen a growing utilization of *in situ* liquid-phase TEM and cryo-TEM, the commonly used standard TEM requires the removal of the suspending liquid after the drop-cast sample preparation. This process is typically realized by vacuum or ambient drying, which often alters the dispersion state of sample materials and introduces artifacts obscuring accurate measurement.[15] All these factors generate discrepancies for representing the size distribution, which can impair comparable and reproducible data analysis.[27] On the other hand, the size distribution observed in TEM results suggested a broader size distribution, evidenced by a higher polydispersity, most notably in MUS-NP2 − NP4. It is important to note that in contrast to SAXS and AUC, TEM measures individual NPs and thus minority size fractions are equally counted and represented, offering an intrinsic advantage for arbitrary populations. On the other hand, thresholding for image contrast may lead to an underestimation of the smaller-sized NPs as the outer part of smaller NPs with poor contrast is typically filtered when applying an overall threshold in common image analysis routines. In spite of these drawbacks, TEM still offers a number of advantages including accessibility and ease of data analysis, thus providing a rapid characterization of AuNP core sizes and shapes, with a semi-quantitative estimation of the degree of homogeneity.[14]

By contrast, both SAXS and AUC are ensemble methods which provides collective data in solution that can be used for detailed statistical analysis of *in situ* colloidal features. Due to the distinct X-ray SLD of gold core and the similar SLD values between alkanethiols and solvent molecules in a AuNP sample, SAXS permits the selective characterization of the gold core while excluding the influence of the ligand shell and the solvation layer. Compared to the results by TEM and AUC, the histograms by MC-SAXS entailed more detailed features of the distribution patterns in both single-type samples and binary mixtures. This can be related to the adequate resolving power of SAXS and the implementation of the unbiased MC modeling, which extends the use of SAXS for non-monodisperse NP systems. It is important to note that the average size in SAXS histograms was slightly larger than those of TEM and AUC for populations with NPs below 3 nm, notably MUS-NP1, MUS-B1 and MUS-B1. These findings are in agreement with the published results on PbS nanocrystals with an unimodal distribution, where larger average size of 3.2 nm for the MC method in comparison to 2.8 nm when fitting the identical SAXS profile with a classical log-normal-based model.[40] Importantly, this discrepancy was markley reduced for samples above 4 nm.[40] This limitation of the MC method for sub-3 nm NPs may be attributed to a number of factors: 1) as described by the Porod's Law, the scattering intensity decreases rapidly at the high q region (corresponding to smaller size), which entails non-negligible systematic data noise; 2) molecules in solution (e.g., salt and solvent) share similar length scales to ultra-small NPs and the scattering of these molecules can not be effectively canceled by solvent subtraction.[12] Once more, this is in line with the PbS study, in which the scattering of unbound lead oleate molecules resulted in a secondary population at 2.3 nm in their MC fitting results.[40] Consequently, the presented MC-SAXS is generally not suitable for characterizing ultra-small AuNPs below 3 nm. Moreover, considering the limit of sample-to-detector distance in SAXS instrumentation as well as the reduced beam flux at the low q region, this MC-SAXS method may not provide accurate estimation of NPs whose diameter above 100 nm without the use of ultra-small angle X-ray scattering (USAXS).

AUC-SV analysis, on the other hand, is a strictly *in situ* process that examines the hydrodynamic behavior of the measured material system. In our experiments, the analysis of 1D sedimentation by a simplified core-shell model resulted in sharp distribution profiles, observed by the pronounced primary peak in both single-type samples and binary mixtures. Consequently, the underrepresentation of minority populations led to an overestimation of the uniformity when compared to SAXS and TEM. This can be explained by the constrained resolution of both AUC measurements and subsequent data fitting. It is important to note that the at times laborious optimization of centrifugation conditions is imperative to achieve a dynamic range covers all species of interest and avoid discrimination of a certain populations.[49] Furthermore, although diluted sample solutions with salt stabilization were used to minimize the charge effects, the concentration dependence of d_{H} could not be completely excluded without the extrapolation to infinite dilutions.[17] The process of extrapolating core sizes from hydrodynamic sizing of 1D sedimentation analysis may also incur systematic errors, especially for non-spherical samples or materials with extended soft shell structures. For such complex systems, more advanced instrumentation, such as multi-wavelength detector, and fitting schemes, e.g. the Custom Grid spectrum analysis, are required to facilitate the implementation of AUC.[25,26,50]

Conclusions

In summary, a comparative study of sub-10 nm AuNP size distribution characterized by TEM, SAXS and AUC is presented. All three methods provided consistent assessment of quasi-monodisperse AuNPs with an average core diameter of 5 nm but distinct differences were observed for non-monodisperse and bimodal populations. The conventional TEM imaging method permitted facile characterization of AuNPs with various size distributions, but it suffered from poor reproducibility and a lack of statistical significance. SAXS measurement, combined with subsequent model-free MC fitting, enabled reliable estimation of non-monodisperse size distributions with comprehensive statistical analysis. However, this method is not suitable for ultra-small NPs below 3 nm due to the reduced scattering intensity and the interference of small molecules. The sedimentation-based AUC-SV method allowed comparable estimation of both single-type samples and binary mixtures. Par contra, its relatively low resolution resulted in the underrepresentation of the minor populations. This study offers valuable insights in state-of-art AuNP characterization methods and may be transferred to guide the size distribution analysis on other material systems.

Acknowledgement

This project received funding from the European Union's Horizon 2020 research and innovation program under grant agreement No. 633635 (DIACHEMO). YY acknowledges the support by the UCL Overseas Research Scholarship and the Graduate Research Scholarship as well as Dr. Han Wu and the EPSRC CNIE research facility service (EPSRC Award, EP/K038656/1) at UCL for the SAXS instrument access. NMF expresses gratitude for funding by the EPSRC under a Doctoral Training Partnership (EP/M507970/1). The authors are grateful to Dr. Paulo Jacob Silva (EPFL) for providing MUS ligand.

Supporting Information Available

The Supporting Information is available free of charge on the ACS Publications website at DOI:

The following files are available free of charge.

- Filename: brief description
- Filename: brief description

References

(1) C. Dreaden, E.; M. Alkilany, A.; Huang, X.; J. Murphy, C.; A. El-Sayed, M. The Golden Age: Gold Nanoparticles for Biomedicine. *Chem. Soc. Rev.* **2012**, *41*, 2740–2779.

(2) Saha, K.; Agasti, S. S.; Kim, C.; Li, X.; Rotello, V. M. Gold Nanoparticles in Chemical and Biological Sensing. *Chem. Rev.* **2012**, *112*, 2739–2779.

(3) Bodelón, G.; Costas, C.; Pérez-Juste, J.; Pastoriza-Santos, I.; Liz-Marzán, L. M. Gold Nanoparticles for Regulation of Cell Function and Behavior. *Nano Today* **2017**, *13*, 40–60.

(4) Burns, A. A.; Vider, J.; Ow, H.; Herz, E.; Penate-Medina, O.; Baumgart, M.; Larson, S. M.; Wiesner, U.; Bradbury, M. Fluorescent Silica Nanoparticles with Efficient Urinary Excretion for Nanomedicine. *Nano Lett.* **2009**, *9*, 442–448.

(5) A. Sousa, A.; A. Hassan, S.; L. Knittel, L.; Balbo, A.; A. Aronova, M.; H. Brown, P.; Schuck, P.; D. Leapman, R. Biointeractions of Ultrasmall Glutathione-Coated Gold Nanoparticles: Effect of Small Size Variations. *Nanoscale* **2016**, *8*, 6577–6588.

(6) Pan, Y.; Neuss, S.; Leifert, A.; Fischler, M.; Wen, F.; Simon, U.; Schmid, G.; Brandau, W.; Jahnen-Dechent, W. Size-Dependent Cytotoxicity of Gold Nanoparticles. *Small* **2007**, *3*, 1941–1949.

(7) Jiang, Y.; Huo, S.; Mizuhara, T.; Das, R.; Lee, Y.-W.; Hou, S.; Moyano, D. F.; Duncan, B.; Liang, X.-J.; Rotello, V. M. The Interplay of Size and Surface Functionality on the Cellular Uptake of Sub-10 nm Gold Nanoparticles. *ACS Nano* **2015**, *9*, 9986–9993.

(8) Macdonald, T. J.; Wu, K.; Sehmi, S. K.; Noimark, S.; Peveler, W. J.; du Toit, H.; Voelcker, N. H.; Allan, E.; MacRobert, A. J.; Gavriilidis, A.; Parkin, I. P. Thiol-Capped Gold Nanoparticles Swell-Encapsulated into Polyurethane as Powerful Antibacterial Surfaces Under Dark and Light Conditions. *Sci. Rep.* **2016**, *6*, 39272.

(9) Schneider, C. A.; Rasband, W. S.; Eliceiri, K. W. NIH Image to ImageJ: 25 years of image analysis. *Nat. Methods* **2012**, *9*, 671–675.

(10) Mondini, S.; Ferretti, A. M.; Puglisi, A.; Ponti, A. Pebbles and PebbleJuggler: software for accurate, unbiased, and fast measurement and analysis of nanoparticle morphology from transmission electron microscopy (TEM) micrographs. *Nanoscale* **2012**, *4*, 5356–5372.

(11) Cho, E. J.; Holback, H.; Liu, K. C.; Abouelmagd, S. A.; Park, J.; Yeo, Y. Nanoparticle Characterization: State of the Art, Challenges, and Emerging Technologies. *Mol. Pharm.* **2013**, *10*, 2093–2110.

(12) Li, T.; Senesi, A. J.; Lee, B. Small Angle X-Ray Scattering for Nanoparticle Research. *Chem. Rev.* **2016**, *116*, 11128–11180.

(13) Modena, M. M.; Rühle, B.; Burg, T. P.; Wuttke, S. Nanoparticle Characterization: What to Measure? *Adv. Mater.* **2019**, *0*, 1901556.

(14) Borchert, H.; Shevchenko, E. V.; Robert, A.; Mekis, I.; Kornowski, A.; Grübel, G.; Weller, H. Determination of Nanocrystal Sizes: A Comparison of TEM, SAXS, and XRD Studies of Highly Monodisperse CoPt3 Particles. *Langmuir* **2005**, *21*, 1931–1936.

(15) Michen, B.; Geers, C.; Vanhecke, D.; Endes, C.; Rothen-Rutishauser, B.; Balog, S.; Petri-Fink, A. Avoiding Drying-Artifacts in Transmission Electron Microscopy: Characterizing the Size and Colloidal State of Nanoparticles. *Sci. Rep.* **2015**, *5*.

(16) Evans, J. E.; Jungjohann, K. L.; Browning, N. D.; Arslan, I. Controlled Growth of Nanoparticles from Solution with In Situ Liquid Transmission Electron Microscopy. *Nano Lett.* **2011**, *11*, 2809–2813.

(17) Dieckmann, Y.; Cölfen, H.; Hofmann, H.; Petri-Fink, A. Particle Size Distribution Measurements of Manganese-Doped ZnS Nanoparticles. *Anal. Chem.* **2009**, *81*, 3889–3895.

(18) Mahl, D.; Diendorf, J.; Meyer-Zaika, W.; Epple, M. Possibilities and Limitations of Different Analytical Methods for the Size Determination of a Bimodal Dispersion of Metallic Nanoparticles. *Colloids Surf. A* **2011**, *377*, 386–392.

(19) Zanchet, D.; Hall, B. D.; Ugarte, D. Structure Population in Thiol-Passivated Gold Nanoparticles. *J. Phys. Chem. B* **2000**, *104*, 11013–11018.

(20) Hall, B. D.; Zanchet, D.; Ugarte, D. Estimating Nanoparticle Size from Diffraction Measurements. *J. Appl. Crystallogr.* **2000**, *33*, 1335–1341.

(21) Calvin, S.; Luo, S. X.; Caragianis-Broadbridge, C.; McGuinness, J. K.; Anderson, E.; Lehman, A.; Wee, K. H.; Morrison, S. A.; Kurihara, L. K. Comparison of Extended X-Ray Absorption Fine Structure and Scherrer Analysis of x-Ray Diffraction as Methods for Determining Mean Sizes of Polydisperse Nanoparticles. *Appl. Phys. Lett.* **2005**, *87*, 233102.

(22) Montes-Burgos, I.; Walczyk, D.; Hole, P.; Smith, J.; Lynch, I.; Dawson, K. Characterisation of Nanoparticle Size and State Prior to Nanotoxicological Studies. *J. Nanoparticle Res.* **2010**, *12*, 47–53.

(23) L. Planken, K.; Cölfen, H. Analytical Ultracentrifugation of Colloids. *Nanoscale* **2010**, *2*, 1849–1869.

(24) Carney, R. P.; Kim, J. Y.; Qian, H.; Jin, R.; Mehenni, H.; Stellacci, F.; Bakr, O. M. Determination of Nanoparticle Size Distribution Together with Density or Molecular Weight by 2D Analytical Ultracentrifugation. *Nat. Commun.* **2011**, *2*, 335.

(25) Demeler, B.; Nguyen, T.-L.; Gorbet, G. E.; Schirf, V.; Brookes, E. H.; Mulvaney, P.; El-Ballouli, A. O.; Pan, J.; Bakr, O. M.; Demeler, A. K.; Hernandez Uribe, B. I.; Bhattarai, N.; Whetten, R. L. Characterization of Size, Anisotropy, and Density Heterogeneity of Nanoparticles by Sedimentation Velocity. *Anal. Chem.* **2014**, *86*, 7688–7695.

(26) Walter, J.; Gorbet, G.; Akdas, T.; Segets, D.; Demeler, B.; Peukert, W. 2D Analysis of Polydisperse Core–Shell Nanoparticles Using Analytical Ultracentrifugation. *Analyst* **2016**, *142*, 206–217.

(27) Chen, Z. H.; Kim, C.; Zeng, X.-b.; Hwang, S. H.; Jang, J.; Ungar, G. Characterizing Size and Porosity of Hollow Nanoparticles: SAXS, SANS, TEM, DLS, and Adsorption Isotherms Compared. *Langmuir* **2012**, *28*, 15350–15361.

(28) Glatter, O. A New Method for the Evaluation of Small-Angle Scattering Data. *J. Appl. Cryst.* **1977**, *10*, 415–421.

(29) Svergun, D. I. Mathematical Methods in Small-Angle Scattering Data Analysis. *J. Appl. Cryst.* **1991**, *24*, 485–492.

(30) Pedersen, J. S. Determination of Size Distribution from Small-Angle Scattering Data for Systems with Effective Hard-Sphere Interactions. *J. Appl. Cryst.* **1994**, *27*, 595–608.

(31) Barteau, K. P.; Ma, K.; Kohle, F. F. E.; Gardinier, T. C.; Beaucage, P. A.; Gillilan, R. E.; Wiesner, U. Quantitative Measure of the Size Dispersity in Ultrasmall Fluorescent Organic–Inorganic Hybrid Core–Shell Silica Nanoparticles by Small-Angle X-Ray Scattering. *Chem. Mater.* **2019**, *31*, 643–657.

(32) Hansen, S.; Pedersen, J. S. A Comparison of Three Different Methods for Analysing Small-Angle Scattering Data. *J. Appl. Cryst.* **1991**, *24*, 541–548.

(33) Martelli, S.; Di Nunzio, P. E. Particle Size Distribution of Nanospheres by Monte Carlo Fitting of Small Angle X-Ray Scattering Curves. *Part. Part. Syst. Charact.* **2002**, *19*, 247–255.

(34) Pauw, B. R.; Pedersen, J. S.; Tardif, S.; Takata, M.; Iversen, B. B. Improvements and Considerations for Size Distribution Retrieval from Small-Angle Scattering Data by Monte Carlo Methods. *J. Appl. Cryst.* **2013**, *46*, 365–371.

(35) Nunzio, P. E. D.; Martelli, S.; Bitti, R. R. Use of Monte Carlo Methods in Characterizing Nanostructured Materials by Wide- and Small-Angle X-Ray Scattering. *J. Dispers. Sci. Technol.* **2005**, *25*, 491–501.

(36) Rosalie, J. M.; Pauw, B. R. Form-Free Size Distributions from Complementary Stereological TEM/SAXS on Precipitates in a Mg–Zn Alloy. *Acta Mater.* **2014**, *66*, 150–162.

(37) Bressler, I.; Pauw, B. R.; Thünemann, A. F. McSAS: Software for the Retrieval of Model Parameter Distributions from Scattering Patterns. *J. Appl. Cryst.* **2015**, *48*, 962–969.

(38) Geertsen, V.; Barruet, E.; Gobeaux, F.; Lacour, J.-L.; Taché, O. Contribution to Accurate Spherical Gold Nanoparticle Size Determination by Single-Particle Inductively Coupled Mass Spectrometry: A Comparison with Small-Angle X-Ray Scattering. *Anal. Chem.* **2018**, *90*, 9742–9750.

(39) Pauw, B. R.; Kästner, C.; Thünemann, A. F. Nanoparticle Size Distribution Quantification: Results of a Small-Angle X-Ray Scattering Inter-Laboratory Comparison. *J. Appl. Cryst.* **2017**, *50*, 1280–1288.

(40) Maes, J.; Castro, N.; De Nolf, K.; Walravens, W.; Abécassis, B.; Hens, Z. Size and Concentration Determination of Colloidal Nanocrystals by Small-Angle X-Ray Scattering. *Chem. Mater.* **2018**, *30*, 3952–3962.

(41) Carney, R. P.; Astier, Y.; Carney, T. M.; Voïtchovsky, K.; Jacob Silva, P. H.; Stellacci, F. Electrical Method to Quantify Nanoparticle Interaction with Lipid Bilayers. *ACS Nano* **2013**, *7*, 932–942.

(42) Yang, Y.; Serrano, L. A.; Guldin, S. A Versatile AuNP Synthetic Platform for Decoupled Control of Size and Surface Composition. *Langmuir* **2018**, *34*, 6820–6826.

(43) Schuck, P. Size-Distribution Analysis of Macromolecules by Sedimentation Velocity Ultracentrifugation and Lamm Equation Modeling. *Biophys. J.* **2000**, *78*, 1606–1619.

(44) Murphy, C. J.; Buriak, J. M. Best Practices for the Reporting of Colloidal Inorganic Nanomaterials. *Chem. Mater.* **2015**, *27*, 4911–4913.

(45) Domingos, R. F.; Baalousha, M. A.; Ju-Nam, Y.; Reid, M. M.; Tufenkji, N.; Lead, J. R.; Leppard, G. G.; Wilkinson, K. J. Characterizing Manufactured Nanoparticles in the Environment: Multimethod Determination of Particle Sizes. *Environ. Sci. Technol.* **2009**, *43*, 7277–7284.

(46) Liu, X.; Atwater, M.; Wang, J.; Huo, Q. Extinction Coefficient of Gold Nanoparticles with Different Sizes and Different Capping Ligands. *Colloids Surf. B* **2007**, *58*, 3–7.

(47) Lechner, M. D.; Cölfen, H.; Mittal, V.; Völkel, A.; Wohlleben, W. Sedimentation Measurements with the Analytical Ultracentrifuge with Absorption Optics: Influence of Mie Scattering and Absorption of the Particles. *Colloid. Polym. Sci.* **2011**, *289*, 1145–1155.

(48) Bekdemir, A.; Stellacci, F. A Centrifugation-Based Physicochemical Characterization Method for the Interaction between Proteins and Nanoparticles. *Nat. Commun.* **2016**, *7*, 13121.

(49) Walter, J.; Peukert, W. Dynamic Range Multiwavelength Particle Characterization Using Analytical Ultracentrifugation. *Nanoscale* **2016**, *8*, 7484–7495.

(50) Walter, J.; Löhr, K.; Karabudak, E.; Reis, W.; Mikhael, J.; Peukert, W.; Wohlleben, W.; Cölfen, H. Multidimensional Analysis of Nanoparticles with Highly Disperse Properties Using Multiwavelength Analytical Ultracentrifugation. *ACS Nano* **2014**, *8*, 8871–8886.

Graphical TOC Entry

Some journals require a graphical entry for the Table of Contents. This should be laid out "print ready" so that the sizing of the text is correct.
Inside the `tocentry` environment, the font used is Helvetica 8 pt, as required by *Journal of the American Chemical Society*.
The surrounding frame is 9 cm by 3.5 cm, which is the maximum permitted for *Journal of the American Chemical Society* graphical table of content entries. The box will not resize if the content is too big: instead it will overflow the edge of the box.
This box and the associated title will always be printed on a separate page at the end of the document.